AIAA JOURNAL
Vol. 44, No. 10, October 2006

Exact Solution of the Bidirectional Vortex

Anand B. Vyas* and Joseph Majdalani†
University of Tennessee Space Institute, Tullahoma, Tennessee 37388

DOI: 10.2514/1.14872

In this paper, we present an inviscid solution that describes the cyclonic motion of a bidirectional vortex in a cylindrical chamber. The study is prompted by the need to characterize the flowfield inside a swirl-driven thrust chamber. This chamber has the advantage of confining mixing and combustion to an inner vortex tube that remains separated from the chamber walls by virtue of an outer stream of swirling, low temperature oxidizer. Our model is based on nonreactive, steady, rotational, axisymmetric, incompressible, and inviscid flow conditions. Unlike other studies of columnar vortices where the axial dependence is not considered, the present model accounts for the chamber's finite body length. In fact, it incorporates the inlet and headwall conditions associated with a swirl-driven cyclone. Based on the resulting formulation, several flow features are captured. Among them is the location of the inner–outer vortex interface where the axial velocity vanishes.

Nomenclature

A_i	=	inlet area
a	=	chamber radius
b	=	chamber outlet radius
l	=	chamber aspect ratio, L/a
p	=	normalized pressure, $\bar{p}/(\rho U^2)$
$\bar{Q}_i$	=	inlet volumetric flow rate
Q_i	=	normalized volumetric flow rate, $\bar{Q}_i/(Ua^2) = \sigma^{-1}$
Re	=	injection Reynolds number, Ua/ν
r	=	normalized radial coordinate, $\bar{r}/a$
S	=	swirl number, $\pi ab/A_i = \pi\beta\sigma$
U	=	mean inlet velocity, $\bar{u}_\theta(a, L)$
$\boldsymbol{u}$	=	normalized velocity $(\bar{u}_r, \bar{u}_z, \bar{u}_\theta)/U$
z	=	normalized axial coordinate, $\bar{z}/a$
β	=	normalized outlet radius, b/a
κ	=	inlet parameter, $Q_i/(2\pi l) = (2\pi\sigma l)^{-1}$
ν	=	kinematic viscosity, μ/ρ
ρ	=	density
σ	=	modified swirl number, $Q_i^{-1} = S/(\pi\beta)$

Subscripts

i, o	=	inlet or outlet property
r	=	radial component or partial derivative
z	=	axial component or partial derivative
θ	=	azimuthal component or partial derivative
$-$	=	overbars denote dimensional variables

I. Introduction

SWIRLING motions have attracted much attention in recent years due to the rich structures that they engender. At one end of the spectrum, one is concerned with understanding, predicting, or controlling the formation of naturally occurring swirl patterns in geophysical phenomena such as whirlpools, tornadoes, dust devils, waterspouts, hurricanes, fire whirls, or cosmic jets (see Penner [1] and Königl [2]). At the other end, one is concerned with the deliberate generation of swirl in thermal and physical transport applications such as cyclonic furnaces and combustors where performance is commensurate with the level of mixing, heat transfer, chemical dispensing, atomization, or filtration.

Unlike columnar vortices, cyclonic flows are characterized by a bidirectional coaxial motion that is not triggered by vortex breakdown or instability. The flow reversal in the conical section of a conventional cyclone may be attributed to the presence of strong centrifugal forces which produce a low pressure region near the chamber axis (see Fig. 1). At the head end, the suction-induced pressure effect draws the primary fluid inwardly and causes it to turn around as the core is approached. The resulting bipolar motion is characterized by the presence of a nontranslating layer separating the upward and downward drafts. This spinning layer is often referred to as the mantle.

One of the earliest investigations of cyclonic motion was carried out by ter Linden [3] whose efforts have focused on determining the influence of geometric parameters on the particle efficiency in dust separators. His experimental work was quickly followed by the treatment of hydraulic and gas cyclones by Kelsall [4] and Smith [5,6], respectively. These experiments were the first to suggest the existence of a forced vortex near the axis of the cyclone. Before these studies, it was widely assumed that a free vortex rather prevailed over the entire chamber volume.

Theoretical analysis of the conical hydrocyclone was initiated using semiempirical approaches by Fontein and Dijksman [7]. It was followed by the momentum-integral analysis of cylindrical gas cyclones by Smith [5,6]. These models were later refined by Bloor and Ingham [8] who employed the Polhausen method to account for inlet flow conditions. Being based on a qualitative knowledge of the flow, the approximate solution by Bloor and Ingham [8] showed good agreement with experimental measurements obtained by Kelsall [4]. Using laboratory tests at the basis of their models, simple mathematical relations were later provided by Reydon and Gauvin [9], Vatistas, Lin and Kwok [10,11], Vatistas [12], and others.

In subsequent years, a simple analytical model for the flow in a conical cyclone evolved from the work of Bloor and Ingham [13]. Unlike earlier studies that had precluded the direct input of inlet conditions, theirs was inviscid and utilized realistic boundary conditions. In their quest for closure, Bloor and Ingham [13] assumed that the mean flow vorticity was everywhere inversely proportional to the distance from the chamber axis. This assumption enabled the extraction of a closed-form approximation for the bulk fluid motion. In fact, Bloor and Ingham's approximation proved useful in reproducing the overall features of the cyclone. Numerical simulations were later carried out by Hsieh and Rajamani [14],

Presented as Paper 5052 at the 39th AIAA/ASME/SAE/ASEE Joint Propulsion Conference and Exhibit, Huntsville, Alabama, 20–23 July 2003; received 23 March 2005; accepted for publication 29 May 2006.

*Graduate Research Associate; currently Visiting Assistant Professor, Department of Mathematical Sciences, University of Delaware, Newark, DE 19716. Member AIAA.

†Jack D. Whitfield Professor of High Speed Flows, Department of Mechanical, Aerospace and Biomedical Engineering. Member AIAA (corresponding author).

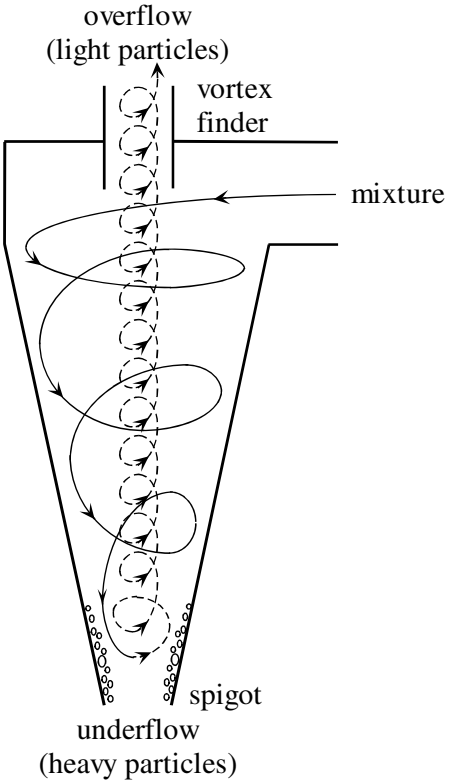

Fig. 1 Sketch of a conical cyclone separator.

Hoekstra, Derksen, and Van den Akker [15], Derksen and Van den Akker [16], and others. Hoekstra and coworkers also conducted laboratory tests using laser-doppler velocimetry (LDV) to verify their multiphase numerical simulations.

While the general interest in improving industrial cyclones continues, the implementation of a fully reversing bidirectional swirl has been recently prompted by a propulsion-related problem. The application in question is concerned with the development of a self-cooled combustion chamber that exhibits several technological advantages. The prototype is due to Chiaverini et al. [17] and consists of an unconventional thrust chamber in which the oxidizer is injected just upstream of the nozzle and tangentially to the inner walls (see Fig. 2). After entering the chamber, the oxidizer spirals toward the head end where fuel is added. Being prevented from crossing the head end, the entrained oxidizer–fuel mixture then reverses direction and spirals inwardly toward the nozzle. The reversed flow is characterized by higher azimuthal velocities.

As in cyclones, a strictly spinning mantle separates the outer updraft from the inner downdraft, thus confining combustion products to the inner vortex tube. The inner swirl increases fuel residence time, turbulence, and propellant mixing, thus improving overall efficiency and thrust. It also allows for shorter chamber lengths. The outer vortex protects the chamber walls from excessive heating loads, thus inducing lower wall temperatures. This feature not only reduces cooling requirements, but also promotes flexibility in material selection, durability and reduced weight (Flinn [18] and Chiaverini et al. [19]).

Unlike cyclonic flows that possess separate outlets for continuous and dispersed phase, the bidirectional coaxial field observed in the cold-wall thrust chamber has only one outlet. To better understand its formation and stability to spatial and periodic disturbances, it would be particularly beneficial if simple forms for the velocity and pressure components could be obtained under steady state conditions. For this reason, it is the purpose of this study to provide closed-form approximations that can be used to describe the bulk gas motion of the bidirectional vortex. The present work summarizes our attempt to provide an inviscid solution to this problem with the aim of confirming its physicality. In this vein, Euler's equations of motion will be used as a starting point.

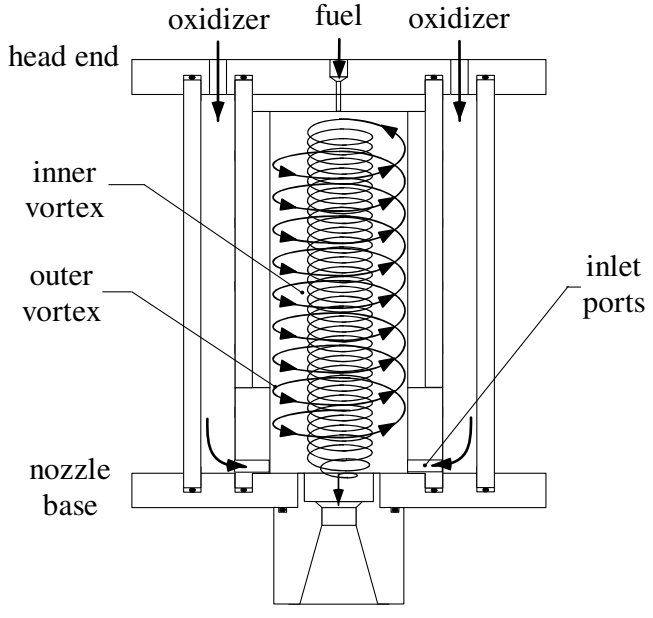

Fig. 2 Sketch of a bidirectional swirl chamber.

II. Mathematical Model

Our idealized chamber is modeled as a cylindrical tube of length L having a closed head end and a partially open downstream end that is attached to a tubular nozzle of radius b. A sketch of the chamber is given in Fig. 3 where $\bar{r}$ and $\bar{z}$ are used to designate the radial and axial coordinates. Note that the nozzle attachment is virtual. The present study is focused on describing the flowfield in the portion of the chamber extending from the head end to the base. Downstream of the base, the flow exits through the virtual nozzle. The fraction of the radius that is open to flow is given by $\beta = b/a$; the chamber's aspect ratio is given by $l = L/a$.

At the base, an aperture in the sidewall permits the tangential injection of an incompressible fluid (i.e., in the azimuthal direction). The assumption of incompressibility is not a restrictive one as the bidirectional vortex has been observed in the flows of both liquids and gases at low speed. The effects of compressibility may become important in the nozzle and are beyond the scope of this study. The forthcoming development is applicable to the bidirectional flow of either a liquid or a gas in the cylindrical portion of the tube ($0 \leq z \leq l$).

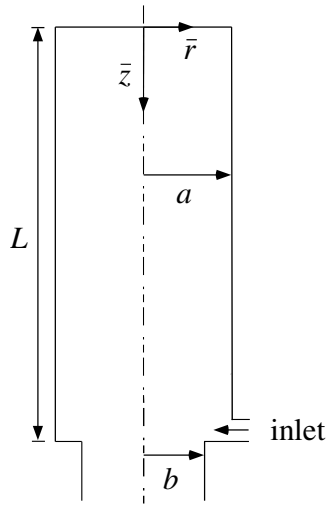

Fig. 3 Idealized chamber and coordinate system.

Because the purpose of the aperture is to permit the tangential injection of the fluid, the axial extent of this aperture is assumed to be small by comparison with the length of the chamber. Without loss in generality, the distribution of this aperture along the tube's circumference may be taken to be uniform, thus mimicking a line source. For an inviscid fluid, the aperture could consist of one or several ports so long as it permits the injection of a rotationally symmetric flow. It must be borne in mind, however, that the actual three-dimensional flow into the chamber will become nearly axisymmetric only after the fluid has traveled some finite distance inside the chamber. In the present model, we ignore this distance needed for axisymmetric flow development.

A. Equations

After entering the chamber, fluid particles follow a helical trajectory traversing the length of the chamber twice before exiting. Because our goal is to quantify the bulk gas motion under moderate to large mean flow Reynolds numbers, the small amount of fuel that is administered at the head end will be ignored in the global flow assessment. The present study will focus on the cold-flow motion that ensues under nonreactive conditions. In summary, our flow will be 1) steady, 2) inviscid, 3) incompressible, 4) rotational, and 5) nonreactive. Under these auspices, simplified equations of motion may be written in standard vector and scalar notations. As usual, continuity may be expressed by $\bar{\nabla}\cdot\bar{\boldsymbol{u}}=0$ or

$$\frac{1}{\bar{r}}\frac{\partial(\bar{r}\bar{u}_r)}{\partial\bar{r}}+\frac{1}{\bar{r}}\frac{\partial\bar{u}_\theta}{\partial\theta}+\frac{\partial\bar{u}_z}{\partial\bar{z}}=0 \tag{1}$$

Similarly, Euler's equation $\rho(\bar{\boldsymbol{u}}\cdot\bar{\nabla}\bar{\boldsymbol{u}})=-\bar{\nabla}\bar{p}$ may be expanded as

$$\bar{u}_r\frac{\partial\bar{u}_r}{\partial\bar{r}}+\frac{\bar{u}_\theta}{\bar{r}}\frac{\partial\bar{u}_r}{\partial\theta}+\bar{u}_z\frac{\partial\bar{u}_r}{\partial\bar{z}}-\frac{\bar{u}_\theta^2}{\bar{r}}=-\frac{1}{\rho}\frac{\partial\bar{p}}{\partial\bar{r}} \tag{2}$$

$$\bar{u}_r\frac{\partial\bar{u}_\theta}{\partial\bar{r}}+\frac{\bar{u}_\theta}{\bar{r}}\frac{\partial\bar{u}_\theta}{\partial\theta}+\bar{u}_z\frac{\partial\bar{u}_\theta}{\partial\bar{z}}+\frac{\bar{u}_\theta\bar{u}_r}{\bar{r}}=-\frac{1}{\rho\bar{r}}\frac{\partial\bar{p}}{\partial\theta} \tag{3}$$

$$\bar{u}_r\frac{\partial\bar{u}_z}{\partial\bar{r}}+\frac{\bar{u}_\theta}{\bar{r}}\frac{\partial\bar{u}_z}{\partial\theta}+\bar{u}_z\frac{\partial\bar{u}_z}{\partial\bar{z}}=-\frac{1}{\rho}\frac{\partial\bar{p}}{\partial\bar{z}} \tag{4}$$

In conformance with previous studies of swirling flows, two further assumptions are made (see Leibovich [20]). The first is that of axisymmetry. The second is actually a byproduct of axisymmetry and frictionless motion. It entails specifying a swirl velocity that is independent of the axial coordinate. In the absence of friction at the wall and between fluid layers, the angular momentum is conserved in the axial direction. At the outset, the sensitivity of the swirl velocity to axial variations becomes immaterial. This result has been routinely adopted in the literature and is well explained in the work of Leibovich [20,21], Beran and Culick [22], Bloor and Ingham [8,13], Vatistas, Lin and Kwok [10,11], Szeri and Holmes [23], and others. Based on these idealizations, the equations of motion become

$$\frac{1}{\bar{r}}\frac{\partial(\bar{r}\bar{u}_r)}{\partial\bar{r}}+\frac{\partial\bar{u}_z}{\partial\bar{z}}=0 \tag{5}$$

$$\bar{u}_r\frac{\partial\bar{u}_r}{\partial\bar{r}}+\bar{u}_z\frac{\partial\bar{u}_r}{\partial\bar{z}}-\frac{\bar{u}_\theta^2}{\bar{r}}=-\frac{1}{\rho}\frac{\partial\bar{p}}{\partial\bar{r}} \tag{6}$$

$$\bar{u}_r\frac{\partial\bar{u}_\theta}{\partial\bar{r}}+\frac{\bar{u}_\theta\bar{u}_r}{\bar{r}}=0 \tag{7}$$

$$\bar{u}_r\frac{\partial\bar{u}_z}{\partial\bar{r}}+\bar{u}_z\frac{\partial\bar{u}_z}{\partial\bar{z}}=-\frac{1}{\rho}\frac{\partial\bar{p}}{\partial\bar{z}} \tag{8}$$

B. Boundary Conditions

The first set of boundary conditions are due to symmetry and the infinite impedance of the walls. The second set is due to the inlet configuration and bulk mass conservation. Physically, these consist of

1) a fully tangential inflow,
2) no axial flow at the head end,
3) no radial flow across the centerline,
4) no radial inflow at the sidewall,
5) an inflow that matches the outflow at the base.

These particular conditions translate into

$$\begin{cases}\bar{u}_\theta(a,L)=U\\ \bar{u}_z(\bar{r},0)=0\\ \bar{u}_r(0,\bar{z})=0\\ \bar{u}_r(a,\bar{z})=0\\ \bar{Q}_o(L)=\bar{Q}_i(L)=UA_i\end{cases} \tag{9}$$

where $\bar{Q}_i$ and $\bar{Q}_o$ represent the inlet and outlet volumetric flow rates. Note that the angular momentum per unit volume is defined by $\mathcal{A}_{\bar{r}}=\rho\bar{r}\bar{u}_\theta$. So given an incompressible and frictionless environment, $\mathcal{A}_{\bar{r}}$ is conserved. This enables us to deduce that the swirl velocity must be inversely proportional to the radius, $\bar{u}_\theta=\mathcal{A}_{\bar{r}}/(\rho\bar{r})\propto\bar{r}^{-1}$. Furthermore, in the injection plane, one gets $\rho aU=\mathcal{A}_a$, and so $\rho aUA_i=\mathcal{A}_aA_i=$ constant. This confirms that the inlet mass flow rate is given by $\dot{m}_i=\rho UA_i=\mathcal{A}_aA_i/a$.

C. Normalization

In seeking a Hiemenz-type similarity solution [24], it is helpful to normalize all variables. Our choice rests on

$$z=\frac{\bar{z}}{a};\qquad r=\frac{\bar{r}}{a};\qquad \nabla=a\bar{\nabla};\qquad \beta=\frac{b}{a} \tag{10}$$

$$u_r=\frac{\bar{u}_r}{U};\qquad u_\theta=\frac{\bar{u}_\theta}{U};\qquad u_z=\frac{\bar{u}_z}{U} \tag{11}$$

$$p=\frac{\bar{p}}{\rho U^2};\qquad Q_i=\frac{\bar{Q}_i}{Ua^2}=\frac{A_i}{a^2};\qquad Q_o=\frac{\bar{Q}_o}{Ua^2} \tag{12}$$

Here $U=\bar{u}_\theta(a,L)=\bar{Q}_i/A_i$ represents the average fluid injection velocity and b refers to the radius of the nozzle. It should be noted that the proper normalization of $\bar{Q}_i$ is not arbitrary, but rather dictated by

$$\frac{\bar{Q}}{Q}=\frac{\int\bar{\boldsymbol{u}}\cdot\hat{\boldsymbol{n}}\,\bar{r}\,\mathrm{d}\bar{r}\,\mathrm{d}\theta}{\int\boldsymbol{u}\cdot\hat{\boldsymbol{n}}\,r\,\mathrm{d}r\,\mathrm{d}\theta}=Ua^2 \tag{13}$$

Another realization is the relation between the normalized volumetric flow rate Q_i and the swirl number S used in the literature. According to the definition proposed by Gupta, Lilley, and Syred [25], and later adopted by Hoekstra, Derksen, and Van den Akker [15], the swirl number appropriate for cyclonic flows may be written as

$$S\equiv\frac{\pi ab}{A_i}=\frac{\pi\beta a^2}{A_i}=\frac{\pi\beta}{Q_i}=\pi\beta\sigma \tag{14}$$

Note that the reciprocal of the normalized volumetric flow rate represents a modified swirl number, $\sigma\equiv Q_i^{-1}$. As expected, the swirl number is increased when the inlet area is reduced at fixed volumetric flow rate.

Pursuant to Eqs. (10–12), the dimensionless conservation equations become

$$\nabla\cdot\boldsymbol{u}=0;\qquad \boldsymbol{u}\cdot\nabla\boldsymbol{u}=-\nabla p \tag{15}$$

After substituting $\boldsymbol{u}\cdot\nabla\boldsymbol{u}=\frac{1}{2}\nabla(\boldsymbol{u}\cdot\boldsymbol{u})-\boldsymbol{u}\times\nabla\times\boldsymbol{u}$ into Eq. (15), one can eliminate the pressure, as usual, by taking the curl of the

momentum equation. This operation yields

$$\nabla \times (\boldsymbol{u} \times \boldsymbol{\Omega}) = 0; \qquad \boldsymbol{\Omega} \equiv \nabla \times \boldsymbol{u} \tag{16}$$

The normalized boundary conditions simplify to

$$\begin{cases} u_\theta(1, l) = 1; & u_z(r, 0) = 0; & u_r(0, z) = 0 \\ u_r(1, z) = 0; & Q_o = \int_0^{2\pi} \int_0^{\beta} \boldsymbol{u}(r, l) \cdot \hat{\boldsymbol{n}}\, r\, \mathrm{d}r\, \mathrm{d}\theta = Q_i \end{cases} \tag{17}$$

where $\boldsymbol{u} \cdot \hat{\boldsymbol{n}} = u_z$ represents the outflow velocity at the base.

III. Solution

Having specified the particular conditions that bring closure to our model, a solution to Eq. (16) may be attempted.

A. Free Vortex

Before proceeding further, it may be helpful to consider the θ-momentum equation. Based on the normalized form of Eq. (7), it can be seen that

$$u_r \left(\frac{\partial u_\theta}{\partial r} + \frac{u_\theta}{r} \right) = 0 \tag{18}$$

One deduces that, regardless of u_r, the azimuthal component must be of the form $u_\theta = A/r$. As explained earlier, the establishment of free vortex motion may be attributed to angular momentum conservation of a frictionless fluid. The first boundary condition in Eq. (17), namely $u_\theta(1, l) = 1$, ensures that the flow enters the chamber tangentially to the inner circumference. One finds $A = 1$ or

$$u_\theta = 1/r \tag{19}$$

Because of the absence of viscous damping near the core, the swirl velocity continues to increase until it becomes unbounded at the chamber axis. This discontinuity is due to the inability of an inviscid model to capture the viscous core interactions that become significant near $r = 0$. The deficiency near the core does not undermine the predictive capabilities elsewhere. Nonetheless, an asymptotic analysis that accounts for the viscous corrections will be needed. Such treatment will be deferred to a later article. The free vortex has an immediate consequence on vorticity. Based on Eq. (19), one is left with

$$\Omega_r = 0; \qquad \Omega_\theta = \frac{\partial u_r}{\partial z} - \frac{\partial u_z}{\partial r}; \qquad \Omega_z = 0 \tag{20}$$

It should be noted that, in practice, the axial component of vorticity will not vanish; instead, it will be concentrated near the chamber axis. In the absence of viscosity, the cancellation of radial and axial vorticity components simplifies the vorticity transport equation given by Eq. (16).

B. Decoupled Equations

Both radial and axial velocity components remain to be determined from the reduced set given by

$$\frac{1}{r} \frac{\partial (r u_r)}{\partial r} + \frac{\partial u_z}{\partial z} = 0 \qquad \text{(continuity)} \tag{21}$$

$$\frac{\partial (u_r \Omega_\theta)}{\partial r} + \frac{\partial (u_z \Omega_\theta)}{\partial z} = 0 \qquad \text{(vorticity transport)} \tag{22}$$

$$\frac{\partial u_r}{\partial z} - \frac{\partial u_z}{\partial r} = \Omega_\theta \qquad \text{(vorticity)} \tag{23}$$

Because of axisymmetry, the introduction of the Stokes stream function is a possibility despite the tridirectionality of the velocity field. As usual, the Stokes stream function ψ can be expressed by

$$u_r = -\frac{1}{r} \frac{\partial \psi}{\partial z}; \qquad u_z = \frac{1}{r} \frac{\partial \psi}{\partial r} \tag{24}$$

When this transformation is used in the vorticity transport equation, one is left with

$$-\frac{\partial \psi}{\partial z} \frac{\partial}{\partial r} \left(\frac{\Omega_\theta}{r} \right) + \frac{\partial \psi}{\partial r} \frac{\partial}{\partial z} \left(\frac{\Omega_\theta}{r} \right) = 0 \quad \text{or} \quad \frac{(\Omega_\theta / r)_z}{(\Omega_\theta / r)_r} = \frac{\psi_z}{\psi_r} \tag{25}$$

The resulting equality will hold if, and only if,

$$\Omega_\theta = r F[\psi(r, z)] \tag{26}$$

By substituting this form into Eq. (25), it can be promptly seen that

$$\frac{(\Omega_\theta / r)_z}{(\Omega_\theta / r)_r} = \frac{[F(\psi)]_z}{[F(\psi)]_r} = \frac{F_\psi \psi_z}{F_\psi \psi_r} = \frac{\psi_z}{\psi_r} \tag{27}$$

where subscripts denote partial derivatives.

C. Vorticity-Stream Function Approach

According to Eq. (26), F can be a general function of ψ. One of the simplest cases corresponds to a linear relation of the form $F = C^2 \psi$; hence, one can put

$$\Omega_\theta = C^2 r \psi \tag{28}$$

This linear choice is guided by the desire to seek an exact solution. It is also inspired by a similar relation used to obtain the bulk gas description in a simulated solid rocket motor (see Culick [26]). Bearing in mind that other possible solutions may exist, we now proceed and substitute Eq. (28) into the remaining vorticity equation given by Eq. (23). At the outset, a linear partial differential equation is precipitated; this is

$$\frac{\partial^2 \psi}{\partial z^2} + \frac{\partial^2 \psi}{\partial r^2} - \frac{1}{r} \frac{\partial \psi}{\partial r} + C^2 r^2 \psi = 0 \tag{29}$$

In turn, the boundary conditions may be conveniently written for the stream function. Based on Eq. (17), one gathers

$$\begin{cases} z = 0; & u_z = 0; & \partial \psi / \partial r = 0 \\ r = 0; & u_r = 0; & \partial \psi / \partial z = 0 \\ r = 1; & u_r = 0; & \partial \psi / \partial z = 0 \\ \int_0^{2\pi} \int_0^{\beta} (\partial \psi / \partial r)\, \mathrm{d}r\, \mathrm{d}\theta = Q_i \end{cases} \tag{30}$$

D. General Solution

Clearly, Eq. (29) is separable. One can proceed by setting $\psi(r, z) = f(r) g(z)$. This decomposes Eq. (29) into

$$-\frac{1}{g} \frac{\mathrm{d}^2 g}{\mathrm{d}z^2} = \frac{1}{f} \left(\frac{\mathrm{d}^2 f}{\mathrm{d}r^2} - \frac{1}{r} \frac{\mathrm{d}f}{\mathrm{d}r} + C^2 r^2 f \right) = \pm \lambda^2 \tag{31}$$

where λ is a separation constant.

For a nonzero λ, the stream function exhibits either trigonometric or hyperbolic variations in the axial direction. Such physical behavior is ruled out. The only plausible choice is attendant on $\lambda = 0$. On the one hand, this value leads to a linear axial variation of the form $g(z) = C_1 z + C_2$. On the other, it permits extracting the radial variation of the stream function from the Bessel equation

$$\frac{\mathrm{d}^2 f}{\mathrm{d}r^2} - \frac{1}{r} \frac{\mathrm{d}f}{\mathrm{d}r} + C^2 r^2 f = 0 \tag{32}$$

such that

$$f(r) = C_3 \sin(\tfrac{1}{2} C r^2) + C_4 \cos(\tfrac{1}{2} C r^2) \tag{33}$$

The general form of the stream function becomes

$$\psi = (C_1 z + C_2)[C_3 \sin(\tfrac{1}{2}Cr^2) + C_4 \cos(\tfrac{1}{2}Cr^2)] \tag{34}$$

E. Particular Solution

Using the constraints associated with Eq. (30) one can evaluate the general constants. Firstly, due to the vanishing axial velocity at the head end, it can be inferred that $C_2 = 0$. This leaves

$$\psi = C_1 z[C_3 \sin(\tfrac{1}{2}Cr^2) + C_4 \cos(\tfrac{1}{2}Cr^2)] \tag{35}$$

Secondly, $u_r(0, z) = 0$ implies that $C_4 = 0$. Thirdly, as u_r vanishes along the sidewall, one must have

$$C_1 C_3 \sin(\tfrac{1}{2}C) = 0 \tag{36}$$

Realizing that neither $C_1 = 0$ nor $C_3 = 0$ are acceptable outcomes, one is left with $\sin(\frac{1}{2}C) = 0$; forthwith, a fundamental solution can be associated with $C = 2\pi$. This gives

$$\psi = Bz \sin(\pi r^2); \qquad B \equiv C_1 C_3 \tag{37}$$

At length, the velocity field reduces to

$$\boldsymbol{u} = -\frac{B}{r}\sin(\pi r^2)\boldsymbol{e}_r + \frac{1}{r}\boldsymbol{e}_\theta + 2B\pi z \cos(\pi r^2)\boldsymbol{e}_z \tag{38}$$

The last constant can be determined from a global mass balance: mass flowing into the chamber must be discharged through the fictitious port of dimensionless radius β. As $Q_o = Q_i$, one must have

$$2\pi \int_0^\beta u_z r \, \mathrm{d}r = Q_i \tag{39}$$

hence,

$$B = Q_i \csc(\pi\beta^2)/(2\pi l) \tag{40}$$

and so

$$\boldsymbol{u} = -\frac{\sin(\pi r^2)}{2\pi\sigma l \sin(\pi\beta^2) r}\boldsymbol{e}_r + \frac{1}{r}\boldsymbol{e}_\theta + \frac{z\cos(\pi r^2)}{\sigma l \sin(\pi\beta^2)}\boldsymbol{e}_z \tag{41}$$

Having formulated the velocity field, the pressure gradients in the radial and axial directions can be deduced. From Eq. (15), one finds

$$\frac{\partial p}{\partial r} = \frac{4\sigma^2 l^2 \pi^2 \sin^2(\pi\beta^2) + \sin^2(\pi r^2) - \pi r^2 \sin(2\pi r^2)}{4\sigma^2 l^2 \pi^2 r^3 \sin^2(\pi\beta^2)} \tag{42}$$

and

$$\frac{\partial p}{\partial z} = -\frac{z \csc^2(\pi\beta^2)}{\sigma^2 l^2} \tag{43}$$

Based on the partial integration of these gradients, the spatial distribution of the pressure may be fully determined.

IV. Discussion

Having obtained the general form of the bidirectional vortex, its distinct flow attributes can be examined. In our problem, the characteristic features of the velocity and pressure profiles can be quantified along the chamber length and cross section by varying the chamber aspect ratio in addition to the inlet and outlet area ratios.

A. Theoretical Location of the Mantle

The mantle represents a nontranslating yet rotating layer that serves to demarcate the axial flow directed toward the head end from that directed toward the nozzle. This layer forms the envelope along which the axial component of the velocity vanishes. It can be determined from the root $r = \beta^*$ for which $\boldsymbol{u}_z = 0$ in Eq. (41). This value can be obtained from

$$Q_i(z/l)\csc(\pi\beta^{*2})\cos(\pi\beta^{*2}) = 0 \tag{44}$$

thus yielding

$$\beta^* = 1/\sqrt{2} \simeq 0.70711 \tag{45}$$

As illustrated in Fig. 4a, the presence of a nontranslating layer at approximately 70.7% of the chamber radius appears to be in excellent agreement with recent CFD results [27,28]. The latter exhibit a vanishing axial velocity at $r \simeq 0.71$. In fact, our theoretical estimate appears to be in agreement with the average value of 0.72 obtained experimentally by Smith [6] in his cylindrical gas cyclone with flat base. Our estimate is also in good agreement with the average value of $\beta^* \simeq 0.675$ predicted by the numerical and experimental studies of Hoekstra, Derksen, and Akker [15]. These tests were carried out at a moderate Reynolds number of $Re = 5 \times 10^4$ and three decreasing swirl numbers of $S = 3.1$, 2.2, and 1.8 (cf. Figs. 5b, 5d, and 5f, p. 2061) [15]. The small deviations from the predicted value of 0.707 may be attributed to the particular use of the Reynolds stress transport model (RSTM) and to geometric differences that are specific to gas cyclones.

In the gas cyclone, for example, the protrusion of a tubular outlet pipe known as the vortex finder aids in guiding the updrift in the vicinity of the head end where the overflow is drawn. Clearly, the

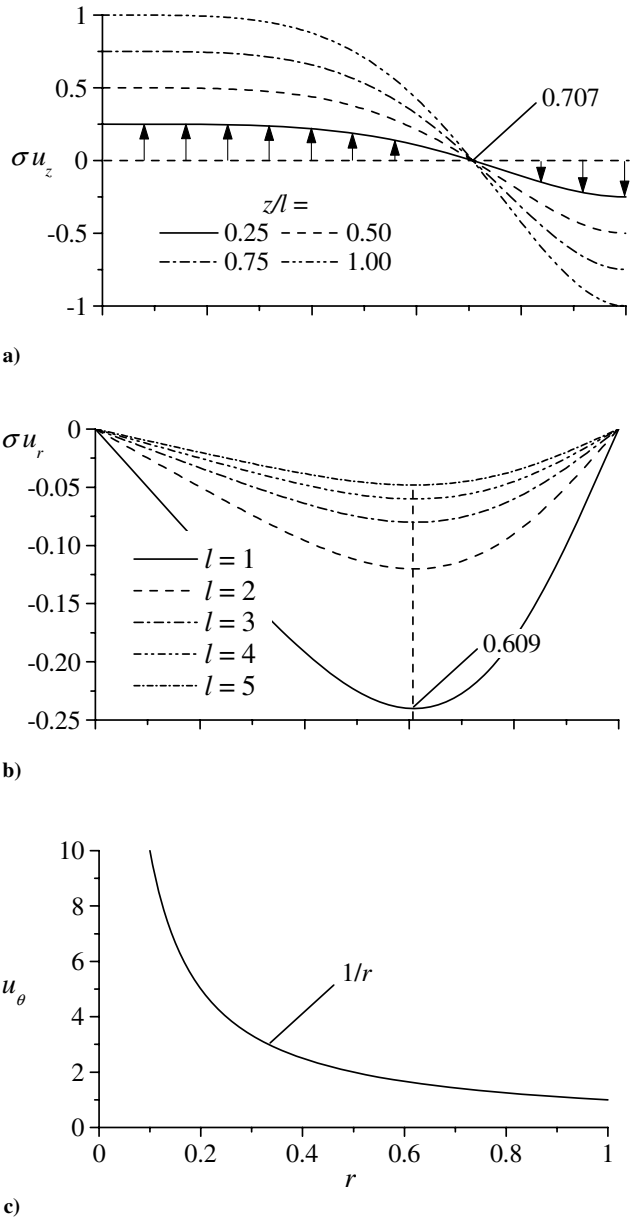

Fig. 4 Axial, radial, and azimuthal (swirl) velocity distributions along the chamber radius.

Table 1 Mantle location by Smith (1962)

Site	$L-\bar{z}$ [in]	$\bar{r}$ [in]	Radial fraction, β^*
1	0.0	2.13	0.7083
2	1.5	2.15	0.7166
3	3.0	2.15	0.7166
4	4.5	2.15	0.7166
5	6.0	2.17	0.7233
6	7.5	2.20	0.7233
7	9.0	2.20	0.7233
Mean		2.16	0.7211

protruding vortex finder can influence the equilibrium position of the mantle. In our model, the vortex finder is replaced by a fictitious tubular nozzle that does not protrude into the chamber. Unlike the cyclonic setup, both inflow and outflow take place at the base of the chamber. In addition to the reversal in the role of gravity on the outgoing motion, our model does not exhibit a secondary outlet to collect the underflow (such as the cyclonic spigot). Despite these basic geometric differences, one should note that the agreement with reported measurements seems to improve at higher Reynolds number [15].

At first glance, the fixed position of the mantle may appear paradoxical, being independent of the inlet flow rate. However, this behavior has been confirmed in a study by Fang [29] who varied the mass flow rate into the chamber by two orders of magnitude without noticing an appreciable change in the average mantle location. For the NASA-ORBITEC subscale vortex engine, the mantle was reported at 0.74 [27].

Theoretically, the spatial determination of the mantle location may be ascribed to mass and momentum balances which, according to our Hiemenz-type similarity solution, will be satisfied when the bidirectional flow is split at $r = 1/\sqrt{2}$. This result has been confirmed experimentally by several reported measurements including those by Smith [6]. One illustrative case is reproduced in Table 1 for a mean flow Reynolds number of 100,000 and several axial positions distributed along the chamber length. Within experimental uncertainty, some of the results obtained by Smith [6] tend to corroborate the theoretical mantle location predicted here.

It may be instructive to note that the weak sensitivity of the mantle location to inlet flow conditions has been confirmed by the numerical experiments of Fang, Majdalani, and Chiaverini [27,28]. Despite the basic geometric differences between their model and ours, a qualitative agreement with their findings could be noted.

B. Ideal Nozzle Opening

When the nozzle radius happens to be smaller than the radius of the inner vortex ($\beta < \beta^*$), a collision can take place between the inner vortex and the wall at $z = l$. This collision can trigger the development of corner flows near the nozzle section. Although corner flows are permitted in the entry section of a real nozzle, they are difficult to capture analytically. The suitability of our mathematical model may hence deteriorate as $\beta^* - \beta$ is increased with successive nozzle area contractions.

When the nozzle opening is allowed to extend beyond the mantle location (for $\beta > \beta^*$), the incoming stream that feeds into the outer vortex cannot be prevented from escaping through the downstream opening. This scenario may be unphysical as it stands to violate global mass conservation. A departure from physicality may be expected with successive increases in $\beta - \beta^*$.

The physical model depicted in Fig. 3 will be optimal when the diameter of the inner vortex matches the diameter of the nozzle. This prevents sudden flow obstructions and unwarranted secondary flows. By setting $\beta = \beta^*$, the outflow will be aligned with the nozzle opening at the base.

C. Velocity and Pressure Relations

By adopting $\beta = \beta^* = 1/\sqrt{2}$, a complete expression for the ideal velocity field may be obtained. In the interest of brevity, we define the geometric inlet parameter

$$\kappa \equiv \frac{Q_i}{2\pi l} = \frac{A_i}{2\pi a L} = \frac{1}{2}\frac{c^2}{a^2}\frac{a}{L} = \frac{1}{2\pi\sigma l} = \frac{a}{2\sqrt{2}LS} \tag{46}$$

where $c = \sqrt{A_i/\pi}$ represents the effective inlet radius. In the practical application that motivates this research, the inlet parameter κ is of order 10^{-2} (one may use $\sigma = 25.6$ and $l = 1$ to find $\kappa = 0.00621$ for the NASA-ORBITEC vortex engine). By virtue of $\beta = 1/\sqrt{2}$, the modified swirl number takes the form

$$\sigma = \frac{1}{Q_i} = \frac{a^2}{A_i} = \frac{\sqrt{2}}{\pi}S \simeq 0.45S \tag{47}$$

The complete bidirectional flow becomes expressible by

$$\begin{cases} \psi = \kappa z \sin(\pi r^2) \\ \boldsymbol{u} = -(\kappa/r)\sin(\pi r^2)\boldsymbol{e}_r + (1/r)\boldsymbol{e}_\theta + 2\pi\kappa z\cos(\pi r^2)\boldsymbol{e}_z \end{cases} \tag{48}$$

The corresponding pressure gradients may be readily determined from Eq. (15), specifically,

$$\frac{\partial p}{\partial r} = \frac{1 + \kappa^2[\sin^2(\pi r^2) - \pi r^2 \sin(2\pi r^2)]}{r^3} \tag{49}$$

$$\frac{\partial p}{\partial z} = -4\pi^2\kappa^2 z \tag{50}$$

To determine the pressure field from Eqs. (49) and (50) partial integration may be performed. At the outset, one finds

$$\Delta p = -\frac{1}{2r^2}\left\{1 + \frac{1}{2}\kappa^2[8\pi^2 r^2 z^2 + 1 - \cos(2\pi r^2)]\right\} \tag{51}$$

where $\Delta p = p - p_0$ and p_0 is the pressure at the head-end center.

D. Confirmation via Energy Conservation

Having obtained an inviscid rotational profile, one expects the sum of the pressure and kinetic energy to remain constant along a streamline. Using normalized quantities, Bernoulli's equation can be written as $p + \frac{1}{2}\boldsymbol{u}\cdot\boldsymbol{u} = H(\psi)$. Based on Eqs. (48) and (51), one finds, after some algebra,

$$H(\psi) = p_0 - 2\pi^2\psi^2 = p + \tfrac{1}{2}\,\boldsymbol{u}\cdot\boldsymbol{u} \tag{52}$$

This confirms that Eq. (48) satisfies Bernoulli's.

E. Cross-Flow Velocity

It should be noted that a constant radial cross-flow velocity $(u_r)_{\text{cross}}$ exists at $r = 1/\sqrt{2}$. This radial influx is uniform along the mantle length and permits mass to be transported to the inner vortex, across the mantle surface. Because of the vanishing axial velocity and inability of the swirl component to transmit mass inwardly, $(u_r)_{\text{cross}}$ provides the only means of communication between the outer and inner vortex regions. Along the mantle interface, the flow is constantly injected into the inner vortex at a rate equal to

$$(u_r)_{\text{cross}} = -\kappa\sqrt{2} = -\frac{1}{\sqrt{2}\pi\sigma l} \qquad \text{(inward)} \tag{53}$$

Interestingly, one may verify that the volumetric cross flow matches the inflow by integrating $(u_r)_{\text{cross}}$ over the mantle length; specifically, one finds

$$2\pi\beta\int_0^l |u_r(\beta, z)|\mathrm{d}z = Q_i \tag{54}$$

F. Axial Velocity Distribution

The axial velocity distribution, described by u_z in Eq. (48), is a linear function of the axial distance from the chamber head end.

Accordingly, the axial velocity linearly decreases as the fluid approaches the head end; conversely, it is seen to accelerate in the downstream direction. This behavior is captured in Fig. 4a where the radial distribution of the axial velocity is shown at several axial stations. As one would expect, the maximum axial velocity is reached at the center of the exit plane $(0, l)$. This maximum velocity can be found to be $(u_z)_{\max} = Q_i$ via Eq. (48). A boundary layer treatment will be required to eliminate the slip flow at the sidewall.

G. Radial Velocity Distribution

A plot of the radial velocity component is given in Fig. 4b for several chamber aspect ratios. Unlike solid or hybrid rocket motors, the radial velocity is zero along the sidewall as there is no gas injection normal to the wall. The radial velocity peaks in the vicinity of the mantle as shown in Fig. 4b. The location of $(u_r)_{\max}$ can be determined numerically or asymptotically from

$$\frac{\mathrm{d}u_r}{\mathrm{d}r} = 0 \quad \text{or} \quad \tan(\pi r_{\max}^2) - 2\pi r_{\max}^2 = 0 \tag{55}$$

Solving Eq. (55) numerically yields $r_{\max} \simeq 0.609106$. This result compares favorably with the computed value of 0.61 based on CFD results obtained by ORBITEC [30]. Forthwith, the largest radial velocity magnitude associated with $r_{\max}$ is found to be

$$(u_r)_{\max} \simeq -1.50879\kappa = -0.24013/(\sigma l) \tag{56}$$

Equation (56) confirms the small size of u_r by comparison with u_z except near the head end where z and thereby u_z approach zero. It also suggests that a smaller radial velocity can be entailed in more elongated chambers or at increasing swirl numbers.

H. Azimuthal Velocity Distribution

Based on Eq. (48), the hyperbolic relation between velocity and radial distance from the chamber axis is illustrated in Fig. 4c. Following the radial velocity behavior, u_θ does not satisfy the no-slip boundary condition at the end wall. Following u_z, u_θ does not vanish along the sidewall. The relaxation of the no-slip condition along the hard walls is consistent with the ideal fluid assumption. Allowing slip does not pose a serious restriction due to the small size of the attendant boundary layers.

I. Flow Streamlines

To aid in flow visualization, the relations needed to trace particle streamlines are determined from Eq. (37) and plotted in Fig. 5 using three increasing lengths corresponding to geometric aspect ratios of $l = 1$, 3, and 5. Because of symmetry about the chamber axis, it is sufficient to describe the flow over half of the domain in a two-dimensional r–z plane. The particle path in a two-dimensional plane can be extended to a three-dimensional domain by superimposing the additional feature of swirl. Note that fluid particles entering the chamber travel along a helical trajectory, reverse direction at the head end, and then return to the nozzle while spinning at higher angular speed. Theoretical patterns are in good agreement with either computational or experimental results obtained by Smith [5,6], Vatistas, Lin, and Kwok [10,11], Hoekstra, Derksen, and Van Den Akker [15], and, lately, by Fang, Majdalani, and Chiaverini [27,28].

J. Chamber Pressure

The radial pressure variation at the chamber head end is illustrated in Fig. 6a. Pressure variations in the axial direction are small and virtually indiscernible from the trends observed at the head end. The head end is chosen because most of the available pressure measurements in the corresponding experiments are acquired at that location. As per Eq. (51), the parabolic decrease in the axial direction is negligible by comparison with radial variations. In practice ($l \geq 1$ and $\sigma \geq 10$), κ is so small that the pressure variation may be accurately approximated by $\Delta p \simeq -1/(2r^2)$ independently of l and σ. Note that the severe depression near $r = 0$ leads to a low pressure

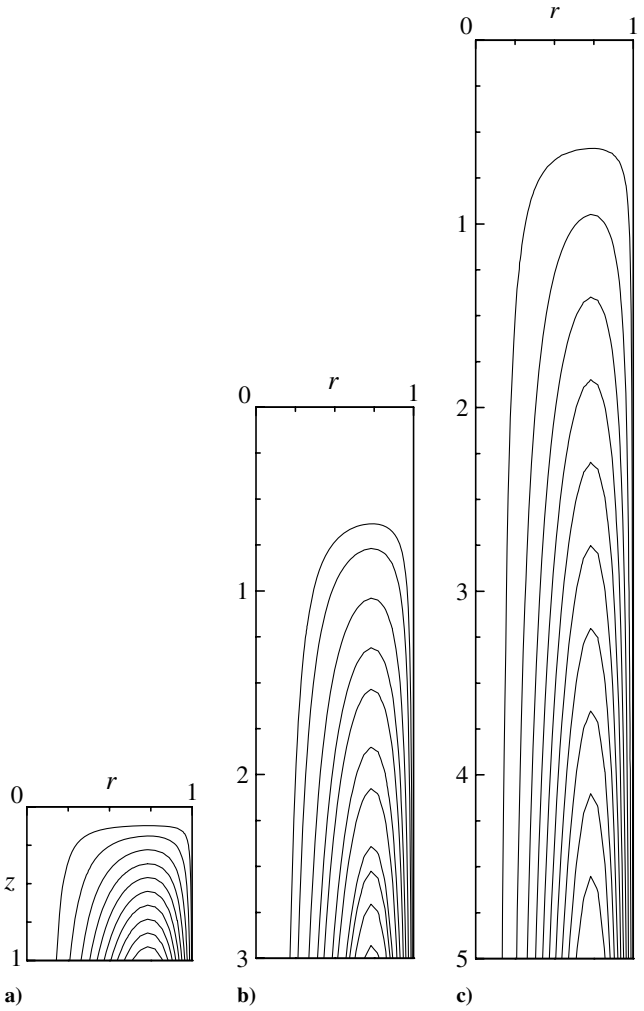

Fig. 5 Streamline patterns at three chamber aspect ratios of a) $L/a = 1$, b) 3, and c) 5. The avoidance of streamlines near the core and head-end regions is to reduce clutter near the wall.

region along the chamber axis that in turn, becomes partly responsible for driving the cyclone.

According to Eq. (49), the radial pressure gradient is invariant to z. This trend is consistent with the behavior of the companion radial velocity. As illustrated in Fig. 6b, the radial pressure gradient is flat near the wall and steep near the core. In the vicinity of the core, a rapid rise in the pressure gradient is observed. The trend depicted in Fig. 6b is, in fact, consistent with recent cold-flow data acquired by Chiaverini and coworkers [30]. Practically, it can be seen from Eq. (49) that $\partial p/\partial r \simeq 1/r^3$ is nearly insensitive to l and σ.

The axial pressure gradient, given by Eq. (50), is plotted in Fig. 6b. In addition to being independent of the radial coordinate, it only varies linearly with the distance from the head end. The small rate of diminution observed in Fig. 6c confirms the slow pressure depreciation in the axial direction. Note that $\partial p/\partial z = -z/(\sigma^2 l^2)$ decreases quadratically with l and σ.

K. Chamber Vorticity

To quantify the rotationality of the flow, it is instructive to evaluate the vorticity distribution in the chamber. Here the vorticity has an azimuthal component only because the flowfield is axisymmetric and both radial and tangential velocities are independent of z. Based on Eqs. (20) and (48), one can write

$$\Omega_\theta = 4\pi^2 \kappa r z \sin(\pi r^2) = 2\pi r z \sin(\pi r^2)/(\sigma l) \tag{57}$$

Figure 7 illustrates the vorticity distribution along the chamber cross section at several axial stations. While the magnitude of Ω_θ

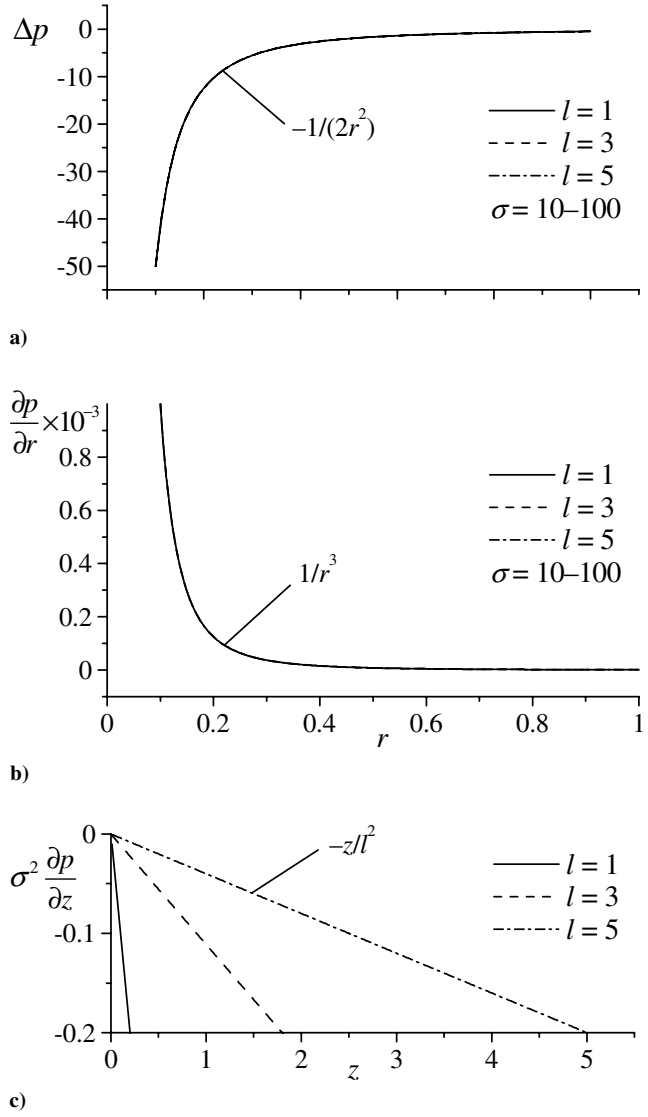

Fig. 6 Variation of a) the head-end chamber pressure and b) its gradient in the radial direction. Also shown in c) is the distribution of the axial pressure gradient along the length of the chamber.

increases linearly along the chamber length, it peaks at a radial position somewhere between the mantle and the wall. Based on Eq. (57), one can calculate the position corresponding to maximum vorticity from the root of $\tan(\pi r_{\max}^2) + 2\pi r_{\max}^2 = 0$. Numerically, one finds $r_{\max} \simeq 0.764596$. This enables us to estimate the largest value of vorticity from

$$\Omega_\theta(r_{\max}, z) \simeq 29.12502 z\kappa = 4.63539 z/(\sigma l) \tag{58}$$

A maximum of $\Omega_{\max} \simeq 4.63539/\sigma$ is realized at $z = l$.

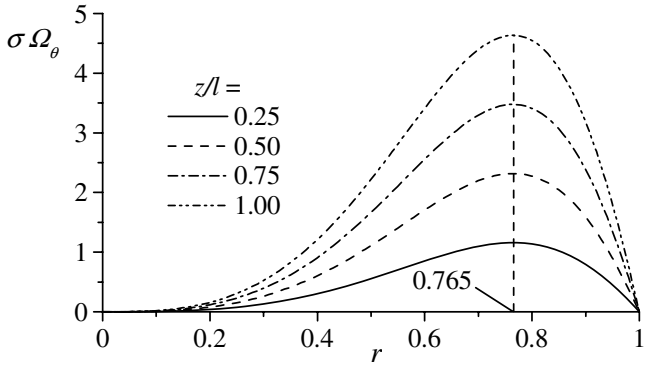

Fig. 7 Radial variation of chamber vorticity at several axial stations.

L. Swirling Intensity

Following Chang and Dhir [31], the swirling intensity for a unidirectional vortex in a pipe of radius a and mean velocity u_m is given by

$$\tilde{\Omega} = \frac{2\pi \int_0^a \rho \bar{u}_z \bar{u}_\theta \bar{r}\, \mathrm{d}\bar{r}}{\rho(\pi a^2)\bar{u}_m^2} \tag{59}$$

Adapting this relation to the problem at hand requires integrating across the outlet flow area. When made dimensionless, the swirling intensity of the flow approaching the outlet may be calculated from

$$\tilde{\Omega} = 4u_m^{-2} \int_0^{1/\sqrt{2}} u_z u_\theta r\, \mathrm{d}r \tag{60}$$

where the mean velocity must be averaged over the outlet area A_b using

$$u_m = \iint_{A_b} A_b^{-1} u_z\, \mathrm{d}A \tag{61}$$

Direct integration yields

$$u_m = (2/\pi) \int_0^{2\pi} \mathrm{d}\theta \int_0^{1/\sqrt{2}} u_z r\, \mathrm{d}r = 8\pi\kappa z \int_0^{1/\sqrt{2}} \cos(\pi r^2) r\, \mathrm{d}r$$
$$= 4\kappa z = 2z/(\pi\sigma l) \tag{62}$$

and so

$$\tilde{\Omega} = \frac{\pi}{2\kappa z} \int_0^{1/\sqrt{2}} \cos(\pi r^2)\, \mathrm{d}r = \frac{\pi}{2\sqrt{2}} \frac{C(1)}{\kappa z} = \frac{\pi C(1)}{(z/l)} S \tag{63}$$

Here $C(x)$ is the Fresnel integral,

$$C(x) \equiv \int_0^x \cos\left(\frac{1}{2}\pi r^2\right) \mathrm{d}r = x - \frac{1}{40}\pi^2 x^5 + \frac{1}{3456}\pi^4 x^9 + \mathcal{O}(x^{13}) \tag{64}$$

The swirling intensity can hence be calculated from

$$\tilde{\Omega} \simeq \frac{0.866244}{\kappa z} = \frac{5.44277}{z} \sigma l = 2.45011 \frac{S}{(z/l)} \tag{65}$$

Clearly, $\tilde{\Omega}$ is largest at the head end and decreases in the downstream direction. This result has important practical implications because it confirms the inception of high mixing rates near the head end. This effect is especially beneficial when cyclonic motion is established under reactive flow conditions involving fuel addition. The large swirling intensity that one may associate with the bidirectional vortex near $z = 0$ gives rise to an optimal reactive flow environment in which rapid burning and increased combustion efficiency may be achieved [19]. For these reasons, the bidirectional vortex appears to be well suited for operation in combustion chambers equipped with head-end fuel injection.

V. Conclusions

Several past investigations have examined the bidirectional motion of a cyclone. While most of these studies have been experimental or numerical in nature, analytical solutions have been largely limited to semiempirical or momentum-integral formulations. In this article, we have constructed a solution directly from Euler's equations. The present application arises in the context of a liquid oxidizer being injected tangentially into a thrust chamber. The resulting flowfield is also applicable to a cylindrical cyclone.

The inviscid flowfield described here exhibits the fundamental characteristics observed in existing laboratory experiments. It also appears to agree with available numerical simulations. Based on the inviscid solution, streamline patterns that bear a striking resemblance to those observed by other investigators are produced. The analytical solution enables us to characterize several key features associated with this problem. For example, the mantle separating the outer and

Table 2 Comparison of the bidirectional vortex and the injection-driven profile by Culick (1966)

Swirl-driven flow: Liquid vortex engine	Injection-driven flow: Solid rocket motor
$\boldsymbol{u} = u_r\boldsymbol{e}_r + u_\theta\boldsymbol{e}_\theta + u_z\boldsymbol{e}_z$	$\boldsymbol{u} = u_r\boldsymbol{e}_r + u_z\boldsymbol{e}_z$
$u_r = -\kappa\sin(\pi r^2)/r$	$u_r = -\sin(\frac{1}{2}\pi r^2)/r$
$u_\theta = 1/r$	$u_\theta = 0$
$u_z = 2\pi\kappa z\cos(\pi r^2)$	$u_z = \pi z\cos(\frac{1}{2}\pi r^2)$
$\boldsymbol{\Omega} = 4\pi^2\kappa r z\sin(\pi r^2)\boldsymbol{e}_\theta$	$\boldsymbol{\Omega} = \pi^2 r z\sin(\frac{1}{2}\pi r^2)\boldsymbol{e}_\theta$
$\psi = \kappa z\sin(\pi r^2)$[a]	$\psi = z\sin(\frac{1}{2}\pi r^2)$

[a] $\kappa = A_i/(2\pi aL) = a/(2\sqrt{2}LS)$.

inner vortex regions is established at 71% of the chamber radius. Former experimental and numerical findings have fallen around this value despite their reliance on averages or regression fits.

Comparatively, the radial velocity is found to be smaller than the axial speed except near the head end where flow turning requires a larger radial component. As predicted by numerical calculations, the maximum radial velocity is reached at $r \simeq 0.61$. Along the length of the chamber, a radial cross flow, albeit small, is seen to exist between the outer and inner vortex regions. The presence of cross flow is confirmed in former tests and computational studies. Mean flow vorticity, on the other hand, reaches its peak value between the mantle and the wall at $r \simeq 0.76$.

While vorticity increases linearly with the distance from the head end, we find the swirling intensity of the inner vortex to depreciate linearly as the nozzle is approached. In similar fashion, we find the pressure to depreciate slowly though quadratically with the distance from the head end. The corresponding pressure gradient, $\partial p/\partial z = -z/(\sigma^2 l^2)$, is slower in longer chambers or in chambers with higher swirl numbers. The axial rate of depreciation is almost insignificant by comparison with the radial rate given by $1/r^3$. The radial depreciation is far more significant to the extent that one may write, $\Delta p \simeq -1/(2r^2)$. Furthermore, the net pressure drop increases with the injection velocity and the distance from the sidewall. The same can be said of the swirl velocity which is accentuated when the injection area ratio is decreased or the distance from the sidewall is increased.

Our mean flow solution is reminiscent of Culick's injection-driven velocity profile [26]; the latter is used to describe the gas motion in an idealized solid rocket motor chamber with circular cross section. The main difference here lies in the presence of a swirl velocity component (see Table 2). Inspired by Culick's profile and its relevance to theoretical studies of core flow motions in solid rocket motors, it may be desirable to study the stability of the bidirectional vortex to temporal disturbances inside vortex-driven liquid rocket engines. One may also wish to investigate the mechanisms of vortex precession and breakdown which have received much attention in the treatment of unidirectional flows.

Acknowledgments

This project is sponsored, in part, by the National Science Foundation and, in part, by NASA/ORBITEC. The authors thank R. Eileen Yingst, Director of the Wisconsin Space Grant Consortium, for the NASA-WSGC Graduate Fellowship and the Faculty Research Infrastructure Awards, respectively. Furthermore, the production of proprietary experimental and numerical data by Martin J. Chiaverini of ORBITEC is most gratefully acknowledged. Last, we thank the Reviewers for their constructive comments and helpful suggestions.

References

[1] Penner, S. S., "Elementary Considerations of the Fluid Mechanics of Tornadoes and Hurricanes," *Acta Astronautica*, Vol. 17, Oct. 1972, pp. 351–362.

[2] Königl, A., "Stellar and Galactic Jets: Theoretical Issues," *Canadian Journal of Physics*, Vol. 64, No. 4, 1986, pp. 362–368.

[3] ter Linden, A. J., "Investigations into Cyclone Dust Collectors," *Proceedings of the Institution of Mechanical Engineers*, Vol. 160, Sept. 1949, pp. 233–251.

[4] Kelsall, D. F., "A Study of Motion of Solid Particles in a Hydraulic Cyclone," *Transactions of the Institution of Chemical Engineers*, Vol. 30, 1952, pp. 87–103.

[5] Smith, J. L., "An Experimental Study of the Vortex in the Cyclone Separator," *Journal of Basic Engineering*, Vol. 84, Dec. 1962, pp. 602–608.

[6] Smith, J. L., "An Analysis of the Vortex Flow in the Cyclone Separator," *Journal of Basic Engineering*, Vol. 84, Dec. 1962, pp. 609–618.

[7] Fontein, F. J., and Dijksman, C., *Recent Developments in Mineral Dressing*, Institution of Mining and Metallurgy, London, 1953, p. 229.

[8] Bloor, M. I. G., and Ingham, D. B., "Theoretical Investigation of the Flow in a Conical Hydrocyclone," *Transactions of the Institution of Chemical Engineers*, Vol. 51, 1973, pp. 36–41.

[9] Reydon, R. F., and Gauvin, W. H., "Theoretical and Experimental Studies of Confined Vortex Flow," *Canadian Journal of Chemical Engineering*, Vol. 59, 1981, pp. 14–23.

[10] Vatistas, G. H., Lin, S., and Kwok, C. K., "Theoretical and Experimental Studies on Vortex Chamber Flows," *AIAA Journal*, Vol. 24, No. 4, 1986, pp. 635–642.

[11] Vatistas, G. H., Lin, S., and Kwok, C. K., "Reverse Flow Radius in Vortex Chambers," *AIAA Journal*, Vol. 24, No. 11, 1986, pp. 1872–1873.

[12] Vatistas, G. H., "Tangential Velocity and Static Pressure Distributions in Vortex Chambers," *AIAA Journal*, Vol. 25, No. 8, 1987, pp. 1139–1140.

[13] Bloor, M. I. G., and Ingham, D. B., "The Flow in Industrial Cyclones," *Journal of Fluid Mechanics*, Vol. 178, May 1987, pp. 507–519.

[14] Hsieh, K. T., and Rajamani, R. K., "Mathematical Model of the Hydrocyclone Based on Physics of Fluid Flow," *AIChE Journal*, Vol. 37, No. 5, 1991, pp. 735–746.

[15] Hoekstra, A. J., Derksen, J. J., and Van den Akker, H. E. A., "An Experimental and Numerical Study of Turbulent Swirling Flow in Gas Cyclones," *Chemical Engineering Science*, Vol. 54, July 1999, pp. 2055–2065.

[16] Derksen, J. J., and Van den Akker, H. E. A., "Simulation of Vortex Core Precession in a Reverse-Flow Cyclone," *AIChE Journal*, Vol. 46, No. 7, 2000, pp. 1317–1331.

[17] Chiaverini, M. J., Malecki, M. J., Sauer, J. A., and Knuth, W. H., "Vortex Combustion Chamber Development for Future Liquid Rocket Engine Applications," AIAA Paper 2002-2149, July 2002.

[18] Flinn, E. D., "Cooling of a Hot New Engine," *Aerospace America*, Vol. 39, Sept. 2001, pp. 26–27.

[19] Chiaverini, M. J., Malecki, M. J., Sauer, J. A., Knuth, W. H., and Majdalani, J., "Vortex Thrust Chamber Testing and Analysis for O2-H2 Propulsion Applications," AIAA Paper 2003-4473, July 2003.

[20] Leibovich, S., "Vortex Stability and Breakdown: Survey and Extension," *AIAA Journal*, Vol. 22, No. 9, 1984, pp. 1192–1206.

[21] Leibovich, S., "The Structure of Vortex Breakdown," *Annual Review of Fluid Mechanics*, Vol. 10, 1978, pp. 221–246.

[22] Beran, P. S., and Culick, F. E. C., "The Role of Non-Uniqueness in the Development of Vortex Breakdown in Tubes," *Journal of Fluid Mechanics*, Vol. 242, Sept. 1992, pp. 491–527.

[23] Szeri, A., and Holmes, P., "Nonlinear Stability of Axisymmetric Swirling Flows," *Philosophical Transactions of the Royal Society of London, Series A: Mathematical and Physical Sciences*, Vol. 326, No. 1590, 1988, pp. 327–354.

[24] Hiemenz, K., "Die Grenzschricht an Einem in den Gleichförmigen Flüssigkeitsstrom Eingetauchten Geraden Kreiszylinder," *Dingler's Polytechnisches Journal*, Vol. 326, No. 22, 1911, pp. 344–348.

[25] Gupta, A. K., Lilley, D. G., and Syred, N., *Swirl Flows*, Abacus, London, UK, 1984.

[26] Culick, F. E. C., "Rotational Axisymmetric Mean Flow and Damping of Acoustic Waves in a Solid Propellant Rocket," *AIAA Journal*, Vol. 4, No. 8, 1966, pp. 1462–1464.

[27] Fang, D., Majdalani, J., and Chiaverini, M. J., "Simulation of the Cold-Wall Swirl Driven Combustion Chamber," AIAA Paper 2003-5055, July 2003.

[28] Fang, D., Majdalani, J., and Chiaverini, M. J., "Hot Flow Model of the Vortex Cold Wall Liquid Rocket," AIAA Paper 2004-3676, July 2004.

[29] Fang, D., "Computational Fluid Dynamics (CFD) Study of Nasa's Cold-Wall Swirl-Driven Rocket Combustion Chamber," M.S. Thesis, Marquette University, 2004.

[30] Chiaverini, M. J., private communication, 2003.

[31] Chang, F., and Dhir, V. K., "Mechanisms of Heat Transfer Enhancement and Slow Decay of Swirl in Tubes with Tangential Injection," *International Journal of Heat and Fluid Flow*, Vol. 16, No. 2, 1995, pp. 78–87.

S. Aggarwal
Associate Editor